Hattermann, T., O. A. Nøst, J. M. Lilly, and L. H. Smedsrud (2012). Two years of oceanic observations below the Fimbul Ice Shelf, Antarctica. *Geophysical Research Letters*, **39**, L12605: 1–6, doi:10.1029/2012GL051012. To view the published open abstract, go to http://dx.doi.org and enter the DOI.

Two years of oceanic observations below the Fimbul Ice Shelf, Antarctica

Tore Hattermann, Norwegian Polar Institute, Fram Centre, Hjalmar Johansens gt. 14, N-9296 Tromsø, Norway (hattermann@npolar.no).

Ole Anders Nøst, Norwegian Polar Institute.

Jonathan M. Lilly, NorthWest Research Associates.

Lars H. Smedsrud, Uni Research and Bjerknes Centre for Climate Research.

Abstract

The mechanisms by which heat is delivered to Antarctic ice shelves are a major source of uncertainty when assessing the response of the Antarctic ice sheet to climate change. Direct observations of the ice shelf-ocean interaction are extremely scarce and in many regions melt rates from ice shelf-ocean models are not constrained by measurements. Our two years of data (2010–2012) from three oceanic moorings below the Fimbul Ice Shelf in the Eastern Weddell Sea show cold cavity waters, with average temperatures of less than 0.1 °C above the surface freezing point. This suggests low basal melt rates, consistent with remote sensing-based, steady-state mass balance estimates for this sector of the Antarctic coast. Oceanic heat for basal melting is found to be supplied by two sources of warm water entering below the ice: (i) eddy-like bursts of Modified Warm Deep Water that access the cavity at depth for eight months of the record; and (ii) fresh surface water with temperatures above freezing that flush parts of the ice base during late summer and fall. This interplay of processes implies that basal melting at the Fimbul Ice Shelf cannot simply be parameterized by coastal deep ocean temperatures, but instead appears directly linked to both solar forcing at the surface as well as to the dynamics of the coastal current system.

1. Introduction

Understanding ice shelf–ocean interaction is a major topic when assessing the future mass budget of the Antarctic Ice Sheet [*Joughin and Alley*, 2011; *Pollard and DeConto*, 2009]. About half of the Antarctic coast is fringed by ice shelves, and nearly 90 % of the continental ice loss is discharged through these floating glaciers into the ocean [*Jacobs et al*., 1992]. Their presence affects the flow of the adjacent grounded ice [*Rignot et al*., 2004], with recent examples of sudden break-up events along the Antarctic Peninsula showing that some ice shelves appear highly sensitive to a changing climate [*Scambos et al*., 2000]. However, direct measurements of ocean properties below the ice are sparse, and in many areas the rates and mechanisms by which oceanic heat reaches the ice are as yet unknown [*Hattermann and Levermann*, 2009; *Hellmer*, 2004].

Jacobs et al. [1992] hypothesized three general modes of heat supply for basal melting. In mode 1, the base of the ice shelf is exposed to waters with temperatures at the surface freezing point, which form a heat source for basal melting at depth, because the freezing point of seawater decreases with increasing pressure. The cavity circulation in this "freezing-point depression" mode is dominated by an upside-down gravity plume that determines the spatial pattern of melting and freezing as it rises along the ice base [*Hellmer and Olbers*, 1989]. Overall basal mass loss in this mode is rather low, with high melt rates confined to the deepest areas near the grounding lines, and potential for marine ice formation over regions of thinner ice [*Jenkins*, 1991]. The two other modes refer to melting caused by direct access of an external warm water source, either due to a warm inflow at depth (mode 2), or due to the interaction of seasonally warmer surface waters with the ice front (mode 3).

Observations verify the presence of the freezing-point depression mode beneath the large ice shelves in the Ross and Weddell Sea [*Nicholls and Makinson*, 1998]. Recent studies furthermore document the direct access of warm water at depth beneath the ice shelves in the

Amundsen and Bellinghausen Seas [*Jenkins et al*., 2010], and it has been suggested that average melt rates are primarily a function of deep open ocean temperatures offshore from the ice edge [*Holland et al*., 2008; *Beckmann and Goosse*, 2003]. However, below most Antarctic ice shelves, the circulation pattern remains completely unknown, with sub-shelf temperatures likely being controlled by a variety of different processes [*Nøst et al*., 2011; *Smedsrud et al*., 2006; *Nicholls*, 1997].

During the Norwegian Antarctic Research Expedition in the austral summer 2009/10, the first hot water drill holes through the main body of the Fimbul Ice Shelf (FIS) were established, in order to directly access the ocean below. Situated at the prime meridian, the oceanographic configuration of the FIS is typical for the ice shelves along the coast of the Eastern Weddell Sea, where only a narrow continental shelf separates the glaciated coast from the warm water of the coastal current. Basal melt rates in this region are highly uncertain. Earlier observations below the FIS were obtained by an autonomous underwater vehicle [*Nicholls et al*., 2006] and from hot water drilling through a sea ice-filled rift near the grounding line [*Nicholls et al*., 2008]. Due to the spatial and temporal limitation of this data, it was not clear whether or not warm waters from the deep ocean may directly enter the ice shelf cavity (see *Price et al*. [2008] and references therein for a summary). Our data provide the first direct observational evidence of a mixture of all three modes of heat supply beneath the FIS, suggesting that basal melting is controlled by a complex interplay of processes. However, the ability of deep warm waters to access the ice cavity appears substantially more constrained than predicted by previous modeling studies.

2. Geographical Setting and Data

A map of Fimbul ice shelf draft and water column thickness as provided by *Humbert* [2010] and *Nøst* [2004] is shown in Figure 1a. The coastal circulation and water masses are primarily controlled by processes within the Antarctic Slope Front (ASF), located at the continental shelf break [*Heywood et al*., 2004]. The largest reservoir of heat within this coastal current system is Warm Deep Water (WDW, see Figure 1 in *Nøst et al*. [2011]), lying just offshore from the ice front at a depth below the shelf break (green line, Figure 1a). Water masses on the continental shelf are referred to as Eastern Shelf Water, with properties being largely determined by the seasonal cycle of surface heat flux and the associated freezing and melting of sea ice [*Nicholls et al*., 2009]. North of the shelf break, the surface water is separated in the vertical from the more saline WDW by a southward deepening pycnocline (forming the ASF). Mixing across this sloping interface produces Modified Warm Deep Water (MWDW) which is transported onshore by an eddy-driven overturning [*Nøst et al*., 2011]. For a more detailed discussion of these and other processes, such as glacial melt water input and coastal polynas, see *Nøst et al*. [2011] and *Nicholls et al,* [2009].

During the 2009/10 expedition, an oceanographic mooring was deployed below the FIS through each of three hot water drill holes. The mooring locations (M1, M2, and M3, Figure 1a) were chosen to sample the most likely pathways along which different water masses may access the cavity. Previous modeling studies show a direct inflow of WDW across the "main sill" near the location of mooring M1 [*Nicholls et al*., 2008; *Smedsrud et al*., 2006]. At about 570 m depth, this sill is the deepest connection of the FIS cavity with the exterior ocean. *Nicholls et al*. [2006] suggested a second inflow across the "eastern sill", (at about 330 m depth) near M3. Finally, the location of M2 was chosen to track the downstream evolution of a possible inflow at M1 into the deep "central basin", which (based on conservation of potential vorticity) may follow contours of constant water column thickness.

Each mooring consists of two Aanderraa RCM9 current meter instruments located at different depths: an upper instrument near the ice base, and a lower one above the seabed, hereafter denoted "M1 upper", "M1 lower", and so forth. At deployment time, CTD profiles were taken with a Seabird SBE49 instrument, calibrated before and after the field campaign.

Hourly time series of horizontal current speed and direction, conductivity, temperature, and dissolved oxygen were retrieved from the moorings during two successive revisits at yearly intervals. Temperature and conductivity time series were calibrated using the initial CTD profiles (no new CTD profiles could be taken as the drill holes were not re-opened). During the first year all sensors returned good data, except for the conductivity measurements from M3, which were unusable. However, during the second year, all conductivity sensors began to experience a significant drift, and we therefore only include the first year in our analysis. Furthermore, we correct the conductivity readings at M1 upper for what we believe to be the effect of frazil ice formation in the sensor, as discussed in the Auxiliary materials. Apart from in Figure 2, all time series shown herein have been smoothened with a 48 hour low-pass filter, in order to remove tidal effects.

Three additional data sets frame our observations: Firstly, ambient water mass properties of the ASF are determined by a set of 44 CTD profiles taken near the FIS-front in 2006 [*Nicholls et al*., 2006], (ASF profiles hereafter). Secondly, the temporal evolution of the coastal hydrography is obtained from a time series of 1094 CTD profiles, collected south of the 2000 m isobath along the coast of Dronning Maud Land over a period of nine months in 2008 by sensor-equipped elephant seals [*Nøst et al*., 2011] (seal data hereafter). Continuous time series were derived from the scattered seal profiles by bin-averaging in temporal (10 day intervals) and vertical (100 m intervals plus the upper 50 m) bins. Only bins with 10 or more good data points were included. Thirdly, average sea ice concentration for 2010–2012 in an approximately 1700 km long belt between 15 °W and 25 °E south of 66 °S has been computed from the AMSR-E/ SSMIS product of sea ice maps [*Spreen et al*., 2008].

3. Results

The vertical structure of our observations below the FIS at each mooring location, together with the potential temperature and salinity CTD profiles are shown in Figure 1b. Box plots of potential temperatures at the moorings show predominantly cold water in the cavity, with average values of less than 0.1 °C above the surface freezing point at all three lower instruments. All upper instruments show average temperatures below the surface freezing point, relating to Ice Shelf Water (ISW) [*Jenkins*, 1991], produced by interaction with the ice base at greater depth. Furthermore, the box plots show the occasional presence of water with temperatures up to several tenths of a degree above the surface freezing point, both at depth and near the ice base. Before analyzing these higher temperature events in more detail, we examine the basic features of the cavity circulation and water masses.

3.1 Circulation and Water Mass Characteristics

The de-tided mean velocity vectors and their associated variance ellipses in Figure 1a illustrate the general sub-shelf circulation. At the two mooring sites close to the ice front, M1 and M3, currents of comparable magnitudes are observed, with average velocities of about 6 cm/s and maxima exceeding 30 cm/s. At M3, a depth-intensified southwestward mean flow along isobaths is observed whereas the observed currents at M1 upper suggests a net outflow of ISW near the ice base. This circulation pattern confirms the inflow across the eastern sill as hypothesized by *Nicholls et al*. [2006] and agrees well with *Price et al*. [2008], who observe most of the ISW north and west of the main sill. By contrast, the deep ocean net exchange across the main sill remains less clear, with the size of the variance ellipse at M1 lower largely exceeding the mean flow. The mean flow at M2 lower indicates a cyclonic circulation following the isobaths of the central basin, while the flow at M2 upper appears to be guided along local ice draft topography that was observed at the drill site with ground penetrating radar (not shown).

In order to identify the origin of the different water masses below the FIS, we compare the sub-ice observations with the hydrography outside the cavity (Figure 2). Typical summertime potential temperature-salinity (T-S) properties over the continental slope are shown by the ASF profiles. Warm and fresh Antarctic Surface Water (ASW) is produced in a thin surface layer by solar heating together with sea ice melt in early summer. During wintertime, this ASW collapses onto Winter Water (WW), a homogeneous water mass with temperatures near the surface freezing point and salinities around 34.3 psu [*Nøst et al*., 2011]. MWDW then corresponds to the mixing line connecting WW with the deeper WDW. The Eastern Shelf Water refers to the coastal composition of the surface waters (ASW and WW) after interacting with glacial melt water and MWDW which has been transported on-shore. During winter, the T-S properties of the Eastern Shelf Water are very similar to those of pure WW and in order to distinguish the seasonal extremes we will use the terms ASW and WW to describe the water masses on the continental shelf.

The color shading in Figure 2 indicates the frequency of occurrence of different water mass T-S properties below the FIS. This histogram is computed by binning the unfiltered time series of all four records at M1 and M2 on a regular grid with a bin size of 0.02 psu and 0.05 °C. Yellow indicates the greatest frequency of observations and the logarithmic color scale is normalized such that a value of one corresponds to the bin with the most readings (containing about 10% of all hourly records). The most frequently occurring water mass below the FIS corresponds to the cold and saline WW. This water mass has temperatures only slightly above the surface freezing point and occupies most of the water column in all CTD profiles and appears to enter the cavity with the continuous inflow observed at the eastern sill (M3). The WW is expected to cause melting mainly at deeper parts of the ice base, where the local freezing-point temperature is depressed below its surface value (by about 0.4 °C at the deepest parts of the ice base, around 500 m depth). This suggests generally low basal melt rates below the FIS with the potential for marine ice production at shallower parts of the ice base. In fact, the CTD profile at M1 reveals a 30 m thick mixed layer at the local freezing point near the ice base as expected in the upper limb of such an ice pump circulation.

In addition, the T-S diagram also shows two other distinct types of warm water occurring less frequently below the ice, visualized in green in the histogram of Figure 2. The first type is a dense water mass with maximum temperatures of -0.6 °C. Its T-S properties clearly resemble the mixing line of the MWDW. We will show that this deep heat source for basal melting enters the cavity mainly across the main sill (at M1 lower). The second type with similar salinities as the ASW and maximum temperatures of -1.6 °C is more buoyant. We will show that this shallow heat source is seasonally present near the ice base at both sites close to the ice front (M1 and M3).

Figure 2 also shows water masses with temperatures below the surface freezing point over a broad range of salinities. We may determine the origin of this ISW, by considering that seawater in contact with the ice base will change its properties by a constant ratio of cooling and freshening as ice melts. In T-S space, this corresponds to a straight "melt water mixing" line that relates ISW with given T-S properties to its source at higher temperatures (see *Nøst and Foldvik* [1994] for details). The melt water mixing lines drawn in Figure 2 identify two different sources for melting below the FIS: (i) ISW derived from the dense MWDW or WW is highlighted by the magenta lines; and (ii) ISW derived from more buoyant water with salinities of the ASW is highlighted by the blue lines. The presence of these two types of ISW indicates that both the shallow and the deep heat source in the cavity contribute to basal melting. We will now analyze these different types heat supply in more detail.

3.2. Warm Surface Water Seasonally Flushes the Ice Base

The time series of temperature, salinity, oxygen, and velocity, recorded below the FIS during 2010–2012 are presented together with the 2008 seal data in Figure 3. The upper instruments at both locations near the ice front (at M1 and M3) exhibit a pronounced seasonality, with warmer water reaching the ice base during the sea ice-free late summer and fall (Figure 3c, right axis). The salinity minimum observed at M1 upper during March and

April 2010 clearly relates this warming signal to the surface-warmed ASW and corresponds well with the fresh coastal water shown by the seal data during this season. We also find evidence that the warm water observed at M3 upper (where no salinity data are available) is likewise derived from ASW. Firstly, the CTD profile taken at M3 in December 2009 shows a warm and fresh layer near the ice base that is consistent with ASW (see inset in Figure 2). Secondly, the co-evolution of temperature and dissolved oxygen at M1 and M3 suggests the same water mass is observed at both locations. The observed increase in dissolved oxygen is also consistent with the warmer water having more recently been ventilated at the ocean surface [*Gammelsrød et al.*, 1994]. This relationship with dissolved oxygen furthermore suggests that the higher temperatures observed in the second year derive from the same source water, although no salinity data are available during that period.

This seasonal inflow of ASW at M1 and M3 directly links basal melting below the FIS to solar heating and indicates the importance of surface processes for ventilating the ice shelf cavities in this sector of Antarctica. To our knowledge, this is the first direct observation of the shallow mode of heat supply for basal melting (mode 3) proposed by *Jacobs et al*. [1992], which has been suggested to influence basal melting at the frontal zones of all Antarctic ice shelves. Our observations show the presence of this shallow heat source up to a distance of 30 km from the ice front (at M3). However, it is not clear how far beyond the mooring locations these buoyant surface waters may penetrate. The brief pulses of warm, fresh and oxygen-rich water observed between April and July 2010 at M2 upper (370 m depth) indicate that the residue of this water mass may travel far into the cavity.

How this buoyant water is depressed more than 150 m beneath the surface, to pass beneath the ice front and into the cavity is an important issue for future research. *Oshima et al*. [1996] argue that the on-shore Ekman transport caused by prevailing eastward winds and the associated downwelling near the ice front is the most likely explanation for this subduction of surface water in the Eastern Weddell Sea. If so, this would imply that the transport of surface water below the FIS is sensitive to surface wind stress and its modulation due to sea ice properties.

3.3. Warm Pulses at Depth

Our observations below the FIS also shed light on the inflow of warm water at depth. In contrast to previous modeling studies, the time series show no signs of a direct inflow of WDW (also clearly evident in the T-S diagram of Figure 2). Instead, a deep heat supply for basal melting is provided by MWDW, a modified version of this water mass, which enters the cavity in transient southward-flowing pulses near the main sill.

These bursts of warm and saline water occur at M1 lower over an eight month period from July 2010 to February 2011, being followed by an increase in mean temperature at all lower sensors, as well as a singular warm event in June 2011. The duration of individual pulses is often shorter than ten hours, and they are contemporaneous with brief periods of large current velocities and increased flow speed variability (Figure 3d). These features lead us to label them “eddies” in a generic sense. Shortly after their occurrence at M1, a similar series of warm pulses is observed “downstream” at the lower sensor of M2, indicating that the MWDW propagates far into the cavity. Most likely, similar pulses also explain the temperature excursions near the grounding line reported by *Nicholls et al*. [2008], showing that MWDW indeed reaches the southern periphery of the cavity where it melts deeper parts of the ice base.

What causes the warm pulses at depth? *Nøst et al*. [2011] argue that mesoscale eddies are important for deep water fluxes within the ASF, and it is reasonable to hypothesize that the observed temperature/current anomalies are the signatures of these features passing the moorings. This is supported by the highly variable flow direction at M1 seen in the large variance ellipses of Figure 1a, since advection of strong eddies past a mooring is associated with rotations of the current vector [*Lilly and Rhines*, 2002]. *Padman et al*. [2009] suggest that tides may be important for the water mass exchange across the continental slope. But the harmonic analysis of our observations [*Pawlowicz,* 2002] yields mean tidal currents at M1 of 2±1 cm/s and maxima rarely exceeding 5 cm/s. Therefore it appears unlikely that tides can be the main mechanism causing the strong pulses observed at M1.

Although the CTD profile at M2 (Figure 1b), which was taken before the occurrence of the warm pulses, suggests that a residual layer of MWDW may permanently fill the deeper parts of the cavity, it remains difficult to estimate the contribution of the warm inflow at depth to the overall heat budget below the FIS. In particular, it remains unclear what controls the occurrence of the pulses that appear to vary interannually, rather than following a clear seasonal cycle. The modeling studies of *Smedsrud et al*. [2006] suggest a strong sensitivity of the inflow at depth to surface wind stress, but further research is needed to understand the dynamics between eddy processes, wind forced-dynamics, tidal effects and interannual variability of the ASF.

4. Conclusions

In this study we have examined two years of oceanic observations below the Fimbul Ice Shelf in order to identify the major heat sources for basal melting. We find that water within the ice shelf cavity is mainly composed of cold Winter Water, which appears to predominately enter the cavity across the eastern sill. In addition, two water masses with temperature above the freezing point occasionally access the cavity, providing heat for basal melting: (i) intermittent bursts of Modified Warm Deep Water that originate within the ambient thermocline, apparently entering the cavity across the main sill; and (ii) fresh Antarctic Surface Water that flushes parts of the ice base with temperatures above freezing during late summer and fall in both years of the record. Unmodified Warm Deep Water is not observed.

Our observations of relatively low temperatures below the FIS are largely consistent with previous snapshots presented by *Nicholls et al*. [2006], suggesting less basal melting than predicted by ocean models [*Nicholls et al*., 2008; *Smedsrud et al*., 2006]. Melt rates below the FIS may thus be consistent with steady state-mass balance estimates based on remote sensing [*Rignot et al*., 2008], indicating that the ice shelves along the coast of Dronning Maud Land are currently not subject to rapid mass loss.

The complex picture emerging from our observations connects basal melting below the FIS both to solar forcing at the surface and to the coastal current dynamics that determine deep water fluxes. This strongly indicates that there is no simple relationship between basal melt rates and deep ocean temperatures or continental shelf width. Instead, the ventilation of the ice shelf cavity involves the interplay of all three modes of heat supply for basal melting discussed by *Jacobs et al*. [1992].

Furthermore, our observations suggest a pronounced seasonal spatial pattern of melting and freezing below the FIS. During winter, when only saline WW or MWDW enter the cavity, melting is mainly limited to greater depth near the grounding line; an associated buoyant plume of ISW may reach all the way to the ice front, potentially producing marine ice at shallower depth. This is opposed by the summer situation, when the plume is separated from the ice base by a layer of much fresher ASW, which prevents refreezing of ISW and leads to melting of shallower ice.

At the moment, we cannot quantify how much the observed deviations from the rather cold mean state alter the total basal mass loss of the ice shelf. It will be necessary to combine observations such as these with theory and numerical modeling in order to advance our understanding of the mechanisms controlling basal melting in the Eastern Weddell Sea. The main issues arising from our results are the indication of an important role for eddy processes in controlling the deep inflow, and new evidence for a shallow source for seasonal basal melt derived from solar warming of the surface layer. Finally, our results imply that the accuracy of simulated basal melt rates will require a proper representation of all coastal processes involved.

Acknowledgments

We thank Keith Nicholls and Keith Makinson for loan of the hot-water-drilling equipment and their intensive advices and support, which made this work possible. Keith Nicholls also provided the ASF profiles. This work was supported by the Centre for Ice, Climate and Ecosystems (ICE) at the Norwegian Polar Institute.

References

Beckmann, A., and H. Goosse (2003), A parameterization of ice shelf-ocean interaction for climate models, *Ocean Model*., 5, 157–170.

Gammelsrød, T., et al.(1994), Distribution of water masses on the continental shelf in the southern Weddell Sea, in *The Polar Oceans and their role in shaping the global environment*, edited by O. M. Johannessen, R. D. Muench, and J. E. Overland, pp. 159–176, American Geophysical Union Geophysical Monograph 85.

Hattermann, T., and A. Levermann (2009), Response of Southern Ocean circulation to global warming may enhance basal ice shelf melting around Antarctica, *Clim. Dyn., 35*(5), 741–756, doi:10.1007/s00382-009-0643-3.

Hellmer, H. H. (2004), Impact of Antarctic ice shelf basal melting on sea ice and deep ocean properties, *Geophys. Res. Lett*., *31* (L10307), doi:10.1029/2004GL019506.

Hellmer, H. H., and D. J. Olbers (1989), A two-dimensional model for the thermohaline circulation under an ice shelf, *Antarct. Sci., 1*(04), 325336.

Heywood, K. J., A. C. Garabato, D. P. Stevens, and R. D. Muench (2004), On the fate of the Antarctic Slope Front and the origin of the Weddell Front, *J. Geophys. Res., 109*, (C06021), doi:10.1029/2003JC002053

Holland, P. R., A. Jenkins, and D. M. Holland (2008), The response of ice shelf basal melting to variations in ocean temperature, *J. Climate., 21*(11), 2558–2572, doi:10.1175/2007JCLI1909.1.

Humbert, A. (2010), The temperature regime of Fimbulisen, Antarctica, *Ann. Glaciol., 51*(55), 5664.

Jacobs, S. S., H. H. Hellmer, C. S. M. Doake, A. Jenkins, and R. M. Frolich (1992), Melting of ice shelves and the mass balance of Antarctica, *J. Glaciol., 38*, 375–387.

Jenkins, A. (1991), A one-dimensional model of ice shelf ocean interaction, *J. Geophys. Res., 96*, 20,671–20,677.

Jenkins, A., P. Dutrieux, S. S. Jacobs, S. D. McPhail, J. R. Perrett, A. T. Webb, and D. White (2010), Observations beneath Pine Island Glacier in West Antarctica and implications for its retreat, *Nat. Geosci., 3,*468-472, doi:10.1038/ngeo890

Joughin, I., and R. B. Alley (2011), Stability of the West Antarctic Ice Sheet in a warming world, *Nat. Geosci., 4*(8), 506–513, doi:10.1038/ngeo1194.

Lilly, J. M., and P. B. Rhines (2002), Coherent eddies in the Labrador Sea observed from a mooring, *J. Phys. Oceanogr., 32*(2), 585–598.

Nicholls, K. (1997), Predicted reduction in basal melt rates of an Antarctic ice shelf in a warmer climate, *Nature, 388*, 460–462.

Nicholls, K.W., and K. Makinson (1998), Ocean circulation beneath the western Ronne Ice Shelf, as derived from in situ measurements of water currents and properties, in *Ocean, ice and atmosphere: Interactions at the Antarctic continental margin, Antarctic Research Series*, vol.75, edited by S. S. Jacobs and R. F. Weiss, pp. 301–318, American Geophysical Union.

Nicholls, K. W., et al. (2006), Measurements beneath an Antarctic ice shelf using an autonomous underwater vehicle, *Geophys. Res. Lett., 33*(L08612), doi:10.1029/2006GL025998.

Nicholls, K. W. , E. P. Abrahamsen, K. J. Heywood, K. Stansfield, and S. Østerhus (2008), High-latitude oceanography using autosub autonomous underwater vehicle, *Limnol. Oceanogr., 53*(5), 2309–2320.

Nicholls, K. W., S. Østerhus, K. Makinson, T. Gammelsrød, and E. Fahrbach (2009), Ice-ocean processes over the continental shelf of the southern Weddell Sea, Antarctica: A review, *Rev. Geophys.*, *47*, 23 PP., doi: 200910.1029/2007RG000250.

Nøst, O. A. (2004), Measurements of ice thickness and seabed topography under the Fimbul Ice Shelf, Dronning Maud Land, Antarctica, *J. Geophys. Res., 109*, C10,010, doi:10.1029/2004JC002277.

Nøst, O. A., and A. Foldvik (1994), A model of ice shelf ocean interaction with application to the Filchner Ronne and Ross ice shelves, J. *Geophys. Res., 99*, 14,243–14,254.

Nøst, O. A., M. Biuw, V. Tverberg, C. Lydersen, T. Hattermann, Q. Zhou, L. H. Smedsrud, and K. M. Kovacs (2011), Eddy overturning of the Antarctic Slope Front controls glacial melting in the Eastern Weddell Sea, *J. Geophys. Res., 116*, C11, 014, doi:10.1029/2011JC006965.

Ohshima, K. I., T. Takizawa, S. Ushio, and T. Kawamura (1996), Seasonal variations of the Antarctic coastal ocean in the vicinity of Lützow-Holm Bay, *J. Geophys. Res.*, *101*(C9), 20,617–20,628.

Padman, L., and R. Erofeeva (2004), A barotropic inverse tidal model for the Arctic Ocean, *Geophys. Res. Lett., 31*(2), Art. No. L02,303.

Padman, L., S. L. Howard, A. H. Orsi, and R. D. Muench (2009), Tides of the north-western Ross Sea and their impact on dense outflows of Antarctic Bottom Water, *Deep-Sea Res. Pt. II, 56*(13-14), 818–834, doi: 10.1016/j.dsr2.2008.10.026.

Pawlowicz, R. (2002), Classical tidal harmonic analysis including error estimates in

MATLAB using T_TIDE, *Computers & Geosciences, 28*, 929–937, doi:10.1016/S00983004(02)00013-4.

Pollard, D., and R. M. DeConto (2009), Modelling West Antarctic Ice Sheet growth and collapse through the past five million years, *Nature, 458*, doi:10.1038/nature07809.

Price, M. R., K. J. Heywood, and K. W. Nicholls (2008), Ice-shelf–ocean interactions at Fimbul Ice Shelf, Antarctica from oxygen isotope ratio measurements, *Ocean Sci*, *4*, 89–98.

Rignot, E., G. Casassa, P. Gogieneni, A. Rivera, and R. Thomas (2004), Accelerated ice discharge from the Antarctic Penninsula following the collapse of Larsen B Ice Shelf, *Geophys. Res. Lett., 31*, DOI: 10.1129/2004GL020,697.

Rignot, E., J. L. Bamber, M. R. van den Broeke, C. Davis, Y. Li, W. J. van de Berg, and E. van Meijgaard (2008), Recent Antarctic ice mass loss from radar interferometry and regional climate modeling, *Nat. Geosci.*, *1*(2), 106–110, doi:10.1038/ngeo102.

Scambos,T., C. Hulbe, M. Fahnestock, and J. Bohlander (2000), The link between climate warming and break-up of ice shelves in the Antarctic Peninsula, *J. Glaciol., 46*, 516–530.

Smedsrud, L. H., A. Jenkins, D. M. Holland, and O. A. Nøst (2006), Modeling ocean processes below Fimbulisen, Antarctica, *J. Geophys. Res., 111*(C01007), doi:10.1029/2005JC002915.

Spreen, G., L. Kaleschke, and G. Heygster (2008), Sea ice remote sensing using AMSR-E 89 GHz channels, *J. Geophys. Res., 113*(C02S03), doi:10.1029/2005JC003384.

Figure Captions

Figure 1. a) Map of Fimbul Ice Shelf, with mooring locations M1, M2, and M3 indicated by red dots, together with water column thickness (gray shading). Black contours show the ice draft in 100 m intervals starting from 250 m. The ice front is shown in magenta,

and the continental shelf break in green (1500 m isobath). Vectors originating at each site show the annual mean value of the 48 hour low-pass filtered currents, surrounded by their associated variance ellipses. A white arrow in the upper right corner indicates the velocity scale. Yellow crosses show the location of individual CTD profiles from the Antarctic Slope Front (ASF) dataset. Gray patches show grounded ice. b) Potential temperature (blue) and salinity (green) profiles measured by the December 2009 drill hole CTD casts, together with boxplots of the low-pass filtered temperature time series for each moored sensor (indicating median, upper and lower quartile, and maximum and minimum temperatures at sensor depth). Maximum temperatures of -1.1°C at M1 lower are off the plot limits, in order to preserve clarity of the CTD profile. Thin vertical lines show the surface freezing point derived from the CTD profiles. Thin horizontal lines indicate ice draft and seabed depth respectively.

Figure 2. Potential temperature-salinity diagram comparing observations below the FIS with coastal hydrography. The color shading shows the relative occurrence of different water masses at the mooring sensors, binned in T-S space, with yellow indicating many observations on a logarithmic scale. Two arrays of meltwater mixing lines, as described in the text, highlight the melting regimes associated with ASW (blue) and MWDW (magenta). The fresh temperature maximum in the CTD profile at M3 (Inset) shows ASW near the ice base at 180 m depth in late December 2009. Contours of constant density are drawn as thin black lines. WW corresponds to the intersection of all three drill hole CTD profiles.

Figure 3. 48-hour low-pass filtered observations of in situ temperature (a), salinity (b), oxygen (c) and current speed (d) below FIS during 2010-2012. Upper-ocean (surface to 250 m) coastal hydrography (a and b) is obtained from the 2008 seal data. Average coastal sea ice concentration (right axis in c) is obtained from AMSR-E/ SSMIS sea ice maps. Current speed (d) is offset in the vertical for presentational clarity, with the time mean value indicated by gray lines. All panels use identical color coding as indicated in (b).

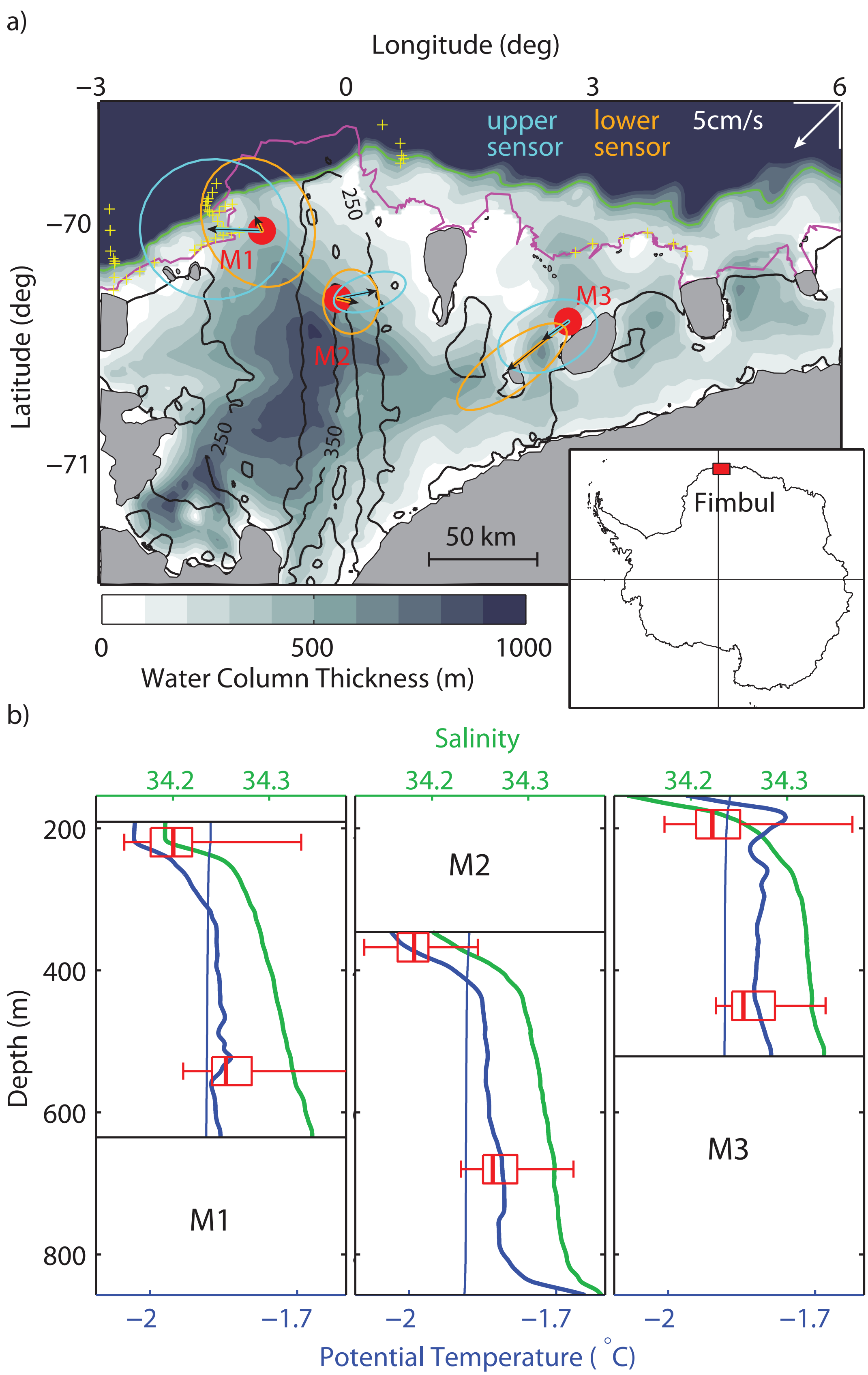
a)
Longitude (deg)
−3
0
3
6
upper sensor
lower sensor
5cm/s
−70
−71
Latitude (deg)
M1
M2
M3
250
350
50 km
Fimbul
0
500
1000
Water Column Thickness (m)
b)
Salinity
34.2
34.3
200
400
600
800
Depth (m)
M1
M2
M3
−2
−1.7
Potential Temperature (°C)

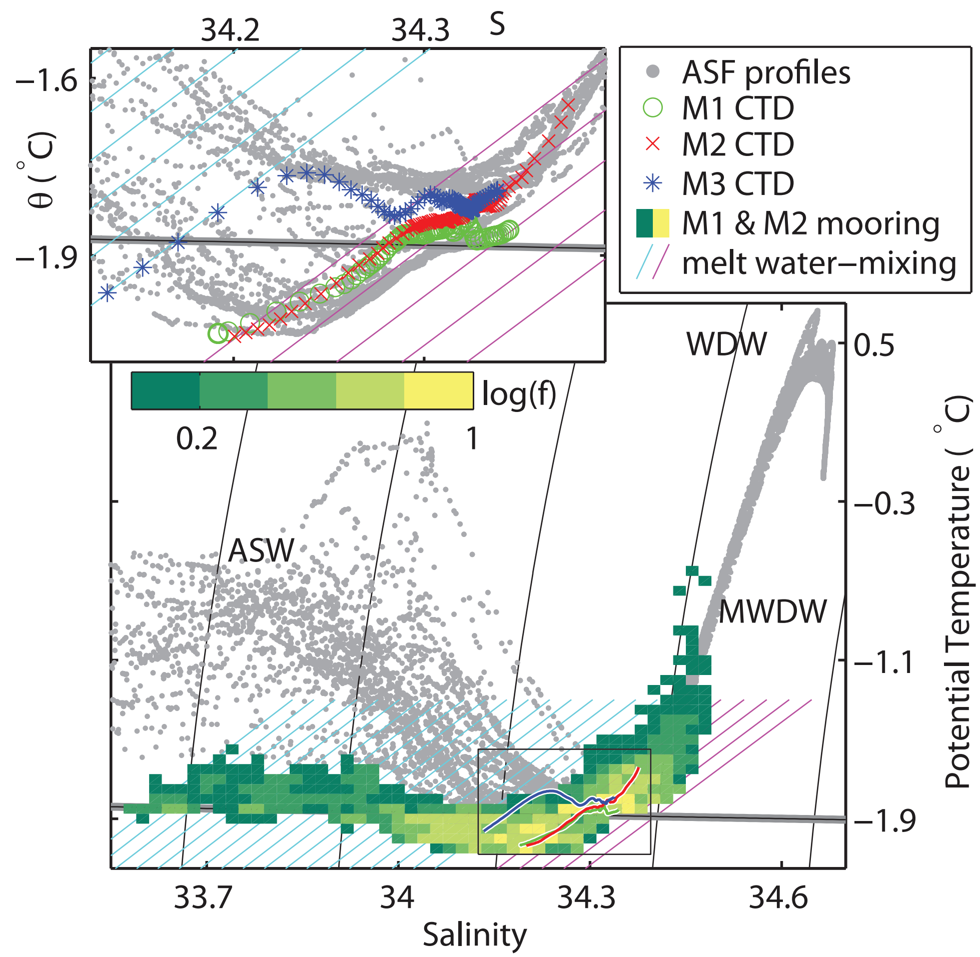

34.2
34.3
S
−1.6
θ (°C)
−1.9
ASF profiles
M1 CTD
M2 CTD
M3 CTD
M1 & M2 mooring
melt water−mixing
log(f)
0.2
1
WDW
ASW
MWDW
0.5
−0.3
−1.1
−1.9
Potential Temperature (°C)
33.7
34
34.3
34.6
Salinity

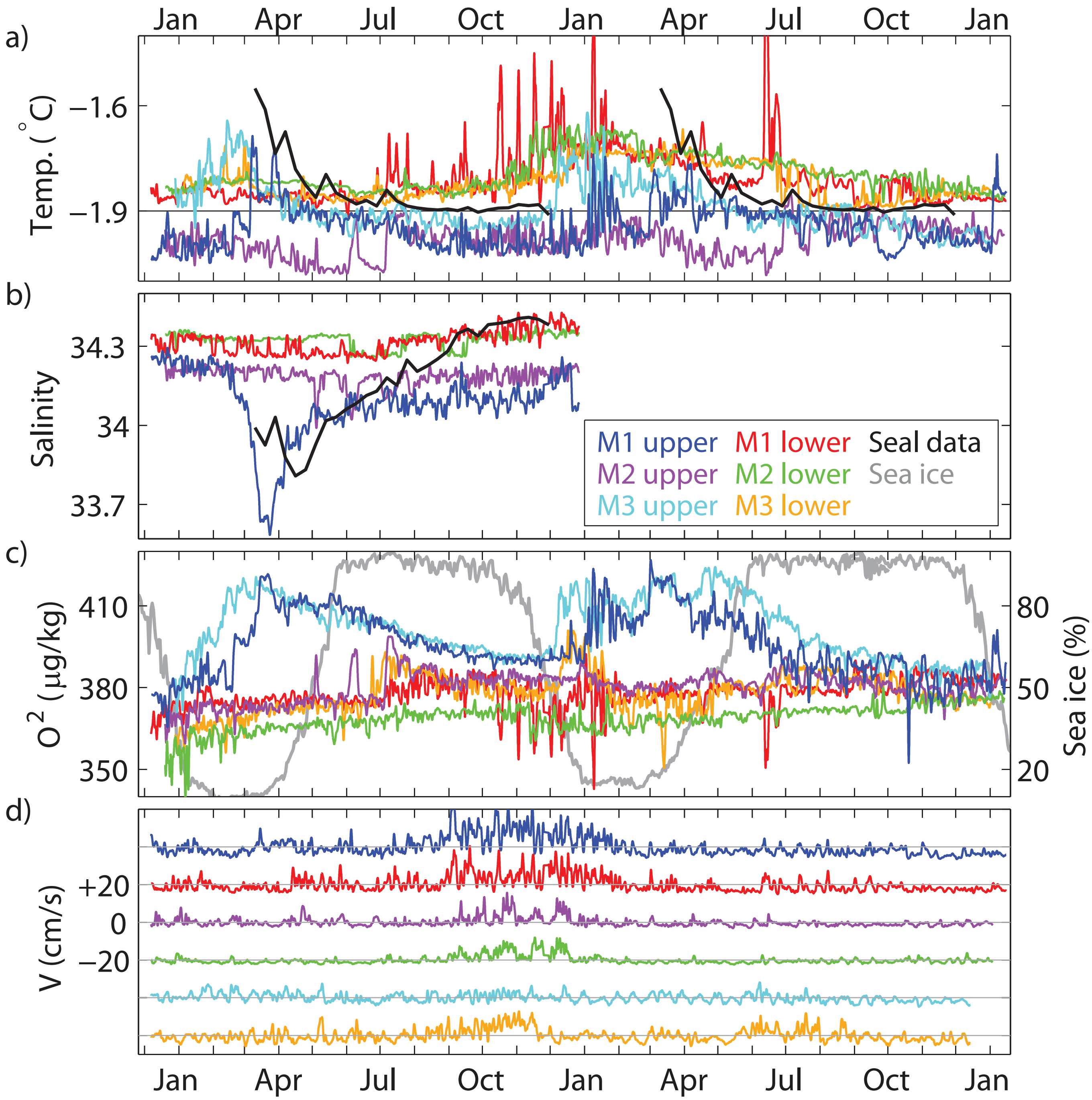

a)
b)
c)
d)
Jan
Apr
Jul
Oct
Jan
Apr
Jul
Oct
Jan
Temp. (°C)
−1.6
−1.9
Salinity
34.3
34
33.7
M1 upper
M1 lower
Seal data
M2 upper
M2 lower
Sea ice
M3 upper
M3 lower
O2 (μg/kg)
410
380
350
Sea ice (%)
80
50
20
V (cm/s)
+20
0
−20